

# Morphology control of metal-modified zirconium phosphate support structures for the oxygen evolution reaction†

Mario V. Ramos-Garcés,<sup>a,b</sup> Joel Sanchez,<sup>ib</sup> c,d Kálery La Luz-Rivera,<sup>a,b</sup>  
Daniel E. Del Toro-Pedrosa,<sup>a</sup> Thomas F. Jaramillo<sup>id</sup> c,d and Jorge L. Colón<sup>id</sup> \*a,b

The electrochemical oxygen evolution reaction (OER) is the half-cell reaction for many clean-energy production technologies, including water electrolyzers and metal–air batteries. However, its sluggish kinetics hinders the performance of those technologies, impeding them from broader implementation. Recently, we reported the use of zirconium phosphate (ZrP) as a support for transition metal catalysts for the oxygen evolution reaction (OER). These catalysts achieve promising overpotentials with high mass activities. Herein, we synthesize ZrP structures with controlled morphology: hexagonal platelets, rods, cubes, and spheres, and subsequently modify them with Co(II) and Ni(II) cations to assess their electrochemical OER behavior. Through inductively coupled plasma mass-spectrometry measurements, the maximum ion exchange capacity is found to vary based on the morphology of the ZrP structure and cation selection. Trends in geometric current density and mass activity as a function of cation selection are discussed. We find that the loading and coverage of cobalt and nickel species on the ZrP supports are key factors that control OER performance.

Received 23rd October 2019,  
Accepted 18th December 2019  
DOI: 10.1039/c9dt04135d

## Introduction

Ever since its crystalline form was reported in 1964,<sup>1</sup> zirconium phosphate nanoparticles have been used for a wide variety of applications. The most extensively studied phase is known as  $\alpha$ -ZrP ( $\text{Zr}(\text{HPO}_4)_2 \cdot \text{H}_2\text{O}$ ); a layered compound with an interlayer distance of 7.6 Å. The classical synthesis of the crystalline form results in particles with a hexagonal-shaped platelet morphology. The structure of  $\alpha$ -ZrP consists of Zr(IV) ions aligning in an imaginary plane bridged by tetrahedral monohydrogen phosphate groups above and below the Zr atom plane. Each Zr(IV) is octahedrally coordinated by six oxygen atoms from six different phosphate groups and three oxygen atoms from each phosphate group are coordinated to different Zr(IV) ions.<sup>2</sup> The fourth oxygen is bonded to an acidic hydrogen atom that is exchangeable by cationic species. This ion exchange property

makes ZrP a suitable support for the incorporation of different species into its layers or on its surface. The resulting composite materials have a wide array of physical properties and can be used for numerous applications.<sup>3</sup> For example, ion-exchanged zirconium phosphate materials have been employed as amperometric biosensors,<sup>4–6</sup> vapochromic materials,<sup>7–9</sup> drug delivery,<sup>10–14</sup> and catalysts.<sup>15–18</sup> Over the last decade, advances in the synthesis of ZrP have resulted in ZrP materials with modified properties (*e.g.*, acidity, surface area, and porosity, among others) and morphologies when compared to pristine  $\alpha$ -ZrP, which have been exploited for different applications.<sup>19–24</sup>

We are interested in an emerging area of application for zirconium phosphate: as a support for electrocatalysts for the oxygen evolution reaction (OER).<sup>25,26</sup> The OER is the oxidative half reaction of water electrolysis, consisting of the four-electron oxidation of water to produce oxygen and protons. It is an important half-cell reaction in many energy related schemes including, but not limited to, photoelectrochemical water splitting, metal–air batteries, and the electrochemical reduction of carbon dioxide.<sup>27</sup> However, the OER suffers from considerable overpotential losses due to its sluggish kinetics, hindering the large-scale implementation of sustainable clean energy production.<sup>28</sup>

Supporting active catalytic species onto supports has been a common strategy to improve activities of various electro-

<sup>a</sup>Department of Chemistry, University of Puerto Rico at Rio Piedras, 17 Ave. Universidad STE 1701, San Juan, PR 00925-2537, USA. E-mail: jorge.colon10@upr.edu

<sup>b</sup>PREM Center for Interfacial Electrochemistry of Energy Materials, University of Puerto Rico, San Juan, PR 00925, USA

<sup>c</sup>Department of Chemical Engineering, Stanford University, Stanford, CA 94305, USA  
<sup>d</sup>SUNCAT Center for Interface Science and Catalysis, Stanford University, CA 94305, USA

† Electronic supplementary information (ESI) available. See DOI: 10.1039/c9dt04135d

catalytic systems.<sup>29–32</sup> Furthermore, nanostructuring of catalysts or support structures has been used to tune catalytic activity.<sup>33–38</sup> Our previous studies indicate that adsorbing Co(II) and Ni(II) cations onto the surface of ZrP nanoparticles and its exfoliated nanosheets result in improved performance over their bulk-intercalated counterparts.<sup>25,26</sup> Herein, we leverage this result to study the surface based catalysis of ZrP materials of various morphologies as supports for Co(II) and Ni(II) species for the OER. More specifically, we synthesize rod-like, cube-like and spherical zirconium phosphate morphologies and ion-exchange their surfaces with Co(II) and Ni(II) cations. These materials were characterized by X-ray powder diffraction (XRPD), Fourier transform infrared spectroscopy (FTIR), transmission electron microscopy/scanning transmission electron microscopy (TEM/STEM), voltammetry, and electrical conductivity measurements. All systems were compared to their sibling hexagonal platelet morphology achieved by  $\alpha$ -zirconium phosphate. We find that all synthesized structures achieve a different maximum ion exchange capacity resulting in unique coverages and loadings of Co and Ni species on ZrP supports. These factors are found to directly impact the activity trends presented below.

## Experimental

### Materials

All chemicals were obtained from commercial sources as analytical or reagent grade and used as received. Cobalt nitrate hexahydrate ( $\text{Co}(\text{NO}_3)_2 \cdot 6\text{H}_2\text{O}$ , 98%), nickel nitrate hexahydrate ( $\text{Ni}(\text{NO}_3)_2 \cdot 6\text{H}_2\text{O}$ , 99.999%), ethanol ( $\text{CH}_3\text{CH}_2\text{OH}$ , 99.5%), 2-propanol ( $(\text{CH}_3)_2\text{CHOH}$ , 99.5%) zirconyl chloride octahydrate ( $\text{ZrOCl}_2 \cdot 8\text{H}_2\text{O}$ , 98%), ammonium fluoride ( $\text{NH}_4\text{F}$ , 99.99%), ammonium phosphate ( $(\text{NH}_4)_2\text{HPO}_4$ , 99.99%), ammonium carbonate ( $(\text{NH}_4)_2\text{CO}_3$ , 99.999%), Nafion 117 (5% solution), and tetradecyltrimethylammonium bromide ( $\text{C}_{17}\text{H}_{38}\text{BrN}$ , TTABr) were obtained from Sigma-Aldrich (St Louis, MO). Phosphoric acid ( $\text{H}_3\text{PO}_4$ , 85%) was obtained from Fischer Scientific (Hampton, NH). Zirconium propionate was supplied by Luxfer MEL Technologies (Flemington, NJ). Vulcan XC-72 (carbon black) was purchased from the Fuel Cell Store (College Station, TX). Glassy carbon rods (SIGRADUR G, HTW Hochtemperatur-Werkstoffe GmbH, 5 mm diameter) were processed by the Stanford University crystal shop to the specifications of a 4 mm height and an area of  $0.196 \text{ cm}^2$ , and the top side was polished to a surface root-mean-square (rms) roughness of  $<50 \text{ nm}$ .

### Synthesis

**$\alpha$ -ZrP (hexagonal platelets).** The synthesis of  $\alpha$ -ZrP was adapted from the literature.<sup>39</sup> 200 mL of a 0.05 M solution of  $\text{ZrOCl}_2 \cdot 8\text{H}_2\text{O}$  was added dropwise to 200 mL of 6 M  $\text{H}_3\text{PO}_4$  that was preheated to  $94 \text{ }^\circ\text{C}$ . This mixture was refluxed at  $94 \text{ }^\circ\text{C}$  for 48 h. The product was then filtered and washed with DI water several times. Finally, it was dried in an oven at  $80 \text{ }^\circ\text{C}$  and grounded into a fine powder with a mortar and pestle.

**Rod-like ZrP.** This synthesis was adapted from the reported minimalistic liquid-assisted route by Cheng *et al.*<sup>23</sup> 1.5137 g of  $\text{ZrOCl}_2 \cdot 8\text{H}_2\text{O}$  were mixed with 175.3 mg of  $\text{NH}_4\text{F}$  (1 : 1 Zr : F ratio) in a beaker. Then, 0.941 mL of  $\text{H}_3\text{PO}_4$  was added to the mixture (Zr :  $\text{H}_3\text{PO}_4$  ratio of 1 : 3) and stirred with a glass rod. This mixture was placed in an oven at  $100 \text{ }^\circ\text{C}$  for 96 h. Finally, the product was washed with DI water several times and dried in an oven at  $60 \text{ }^\circ\text{C}$ .

**Cube-like ZrP ( $\tau'$ -ZrP).** The  $\tau'$  phase of ZrP was reported in 2015 to have a cube-like morphology.<sup>24</sup> 0.726 g of zirconium propionate were dissolved in 10 mL of ethanol. Then, 1.35 mL of  $\text{H}_3\text{PO}_4$  was added to the zirconium propionate solution under stirring. After 15 min, the gel product was washed with ethanol 3 times. The obtained gel was placed in an oven at  $120 \text{ }^\circ\text{C}$  for 18 h. Finally, the product was washed once more with ethanol and dried in an oven at  $78 \text{ }^\circ\text{C}$  overnight.

**Spherical ZrP.** The synthesis of spherical zirconium phosphate was adapted from the literature.<sup>22</sup> More specifically, 1.7908 g of  $\text{ZrOCl}_2 \cdot 8\text{H}_2\text{O}$  were dissolved in 100 mL of  $\text{H}_2\text{O}$ . Then, 3.7750 g of  $(\text{NH}_4)_2\text{CO}_3$  was added under stirring and left for 25 min until the solution became clear. 1.4681 g of  $(\text{NH}_4)_2\text{CO}_3$  was then added to the reaction mixture, followed by 0.6080 g of TTABr. After *ca.* 15 minutes, the reaction was placed in an oven at  $80 \text{ }^\circ\text{C}$ , followed by aging in an autoclave at  $90 \text{ }^\circ\text{C}$  for 48 h, and finally at  $120 \text{ }^\circ\text{C}$  for 24 h. After cooling the reaction product, it was washed with DI water several times. Finally, the solid was placed in a furnace and calcined at  $540 \text{ }^\circ\text{C}$  for 6 h.

**Metal-modified ZrP.** All metal modifications were performed in the same manner for all morphologies. A 2.5 mL solution of the metal salt precursor ( $\text{Co}(\text{NO}_3)_2 \cdot 6\text{H}_2\text{O}$  or  $\text{Ni}(\text{NO}_3)_2 \cdot 6\text{H}_2\text{O}$ ) was added to a 2.5 mL suspension of the ZrP structures and left stirring for 24 h. The metal to ZrP ratio (M : ZrP) was 10 : 1. The products were washed several times with DI water and dried in an oven at  $60 \text{ }^\circ\text{C}$  overnight.

### Electrochemical measurements

Electrochemical measurements were performed on a VMP3 potentiostat/galvanostat (BioLogic Science Instruments). 4-Point probe measurements were conducted on compressed catalyst powders (15 mg in a 6 mm diameter die at 2000 lbs of applied load) using an in-line four-point probe with 1 mm tip spacing (Lucas Labs, Pro4-4000) connected to the VMP3 potentiostat. Oxygen evolution catalytic studies were carried out on a three-electrode electrochemical cell using a rotating disk electrode (RDE) assembly (Pine Research Instrumentation). OER measurements were performed between 0.2 and 1.0 V *versus* the silver/silver chloride couple ( $\text{Ag}/\text{AgCl}$ ) at  $20 \text{ mV s}^{-1}$  in  $\text{O}_2$ -saturated 0.1 M KOH electrolyte with an  $\text{Ag}/\text{AgCl}$  reference electrode (Fisherbrand accumet Glass Body  $\text{Ag}/\text{AgCl}$  Reference Electrode – Mercury-Free, Thermo Fischer). The counter electrode was a platinum wire and the working electrode was a clean, mirror finish-polished, 5 mm diameter glassy carbon disk (GCD) modified with the metal-modified ZrP catalysts. Modification of the GCD with the ZrP catalysts was performed by spin drying a 10  $\mu\text{L}$  drop of an isopropanol, carbon black,

Nafion 117, and ZrP catalyst ink (*vide infra*) at 600 rpm. After drying, the working electrode was composed of a thin coating of the material supported onto the GCD. The total catalyst loading of the working electrode was  $100 \mu\text{g cm}^{-2}$  of material, including the ZrP support. During electrochemical measurements, the working electrode was rotated at 1600 rpm. The rotation speed was fast enough to help in product removal from the surface and limit the bubble formation from oxygen evolution. The solution resistance of the cell was measured at 100 kHz with 20 mV amplitude about the open-circuit potential (OCP), and *iR*-drop compensation occurred after electrochemical testing. The typical solution resistance varied from 40 to 50  $\Omega$ . All potentials were converted and reported herein *versus* the reversible hydrogen electrode (RHE).

The catalytic activity was also determined through a Tafel analysis. Tafel plots were constructed for each system from voltammetry data. The Tafel slopes were determined from the linear region of the plot.

**Ink preparation.** Each catalyst ink was prepared by dispersing 5 mg of the catalyst and 2.5 mg of carbon black in 2.55 mL of isopropanol and 10.02  $\mu\text{L}$  of Nafion 117.<sup>26</sup> The ink was sonicated until it was well dispersed (*ca.* 30 min).

### Chemical and physical characterization

XRPD data were obtained using a Rigaku (Tokyo, Japan) SuperNova single crystal X-ray diffractometer in micro-diffraction mode with Cu  $K\alpha$  radiation ( $\lambda = 1.5417 \text{ \AA}$ ) equipped with a HyPix3000 X-ray detector in transmission mode operated at 50 kV and 1 mA. Measurements were collected at 300 K from  $5^\circ$  to  $40^\circ$  (in the  $2\theta$  axis) using the fast phi move experiment for powders. The *d* spacing was calculated using Bragg's law ( $n\lambda = 2d_{hkl} \sin \theta$ ), where  $\lambda$  is the wavelength of the X-ray source,  $d_{hkl}$  is the interlayer distance between planes in the unit cell, and  $\theta$  is the diffraction angle. Scanning electron microscopy-Energy dispersive spectroscopy (SEM-EDS) was performed on a JEOL (Massachusetts, USA) JSM-6480LV scanning electron microscope. The samples were coated with gold prior to analysis. The morphology of the ZrP structures was also studied by TEM/STEM using a FEI Tecnai (Thermo Fisher Scientific, Inc.) G2F20 TEM/STEM microscope operated at 200 kV. Quantitative determination of the cobalt and nickel loading on the modified ZrP catalysts was done by inductively coupled plasma mass spectrometry (ICP-MS) measurements. Samples were analyzed in a Thermo Fischer Scientific (Waltham, MA) XSeries 2 ICP-MS, and all standard solutions (Co and Ni) were TraceCERT certified and obtained from Sigma-Aldrich. All samples were digested in an aqua regia matrix overnight and were diluted and filtered to a 5 vol% acid concentration for analysis. Vibrational spectroscopy data was obtained from 4000 to  $400 \text{ cm}^{-1}$  using a Bruker (Bruker Optics, Massachusetts, USA) Tensor 27 FT-IR spectrometer with Helios ATR attachment containing a diamond crystal. High resolution X-ray photoelectron spectroscopy (XPS, PHI 5000 VersaProbe) with an Al  $K\alpha$  source was performed. All spectra were calibrated to the adventitious carbon 1s peak at 284.8 eV and fitted using a Shirley background.

## Results and discussion

### XRPD

Fig. 1 shows the XRPD patterns of the four synthesized ZrP structures. The diffraction pattern of  $\alpha$ -ZrP shows the characteristic peaks that correspond to its crystalline structure. Using Bragg's law, the lowest angle diffraction peak corresponding to reflections from the (002) planes indicate an interlayer distance of 7.6  $\text{\AA}$ , as expected.<sup>20</sup> The peaks at *ca.*  $34^\circ$ , which corresponds to the (020) and (31 $\bar{2}$ ) reflections, indicate that an  $\alpha$ -like arrangement of layers is obtained, since they correspond to the Zr-Zr separation within a  $\alpha$ -ZrP layer.<sup>41</sup> The synthesis of the ZrP rods was adapted from the literature;<sup>23</sup> the diffraction pattern is comparable to that of  $\alpha$ -ZrP, with a slightly reduced interlayer distance of 7.4  $\text{\AA}$ . Specifically, pristine ZrP rods are crystalline and contain an  $\alpha$ -like layer arrangement as suggested by the positions of the (002), (020), and (31 $\bar{2}$ ) planes.<sup>23</sup> The slightly reduced interlayer spacing is due to an extended heating period of 100  $^\circ\text{C}$  where the evaporation of interlayer water produces a partially dehydrated phase of  $\alpha$ -ZrP. The loss of water can be observed by FT-IR (*vide infra*). Since the synthesis involves  $\text{NH}_4^+$  cations, their intercalation is possible within this structure. However, the XRPD pattern shows the absence of a shift to lower angles of the lowest angle diffraction peak, indicating that no intercalation of  $\text{NH}_4^+$  cations occurred. The synthesis of ZrP spheres following the Tarafdar *et al.* procedure produced a material with the expected X-ray diffraction pattern<sup>22</sup> for angles larger than  $5^\circ$  shown in Fig. 1, as expected for a material that has been previously determined to be mesoporous by TEM.<sup>22</sup>

In 2015, the phase resulting from the synthesis method that produces cube-like ZrP was found to be similar to a previously reported phase of ZrP called  $\tau$ -ZrP with a few discrepancies.<sup>24</sup> For this reason, this new phase was labelled as  $\tau'$ -ZrP.<sup>24</sup> This phase was described to have Zr octahedrally coordinated by six  $\text{HPO}_4$  tetrahedra forming eight-membered rings. These eight-membered rings contain two P-OH groups pointing to the same side of the Zr plane. The description of the 3D struc-

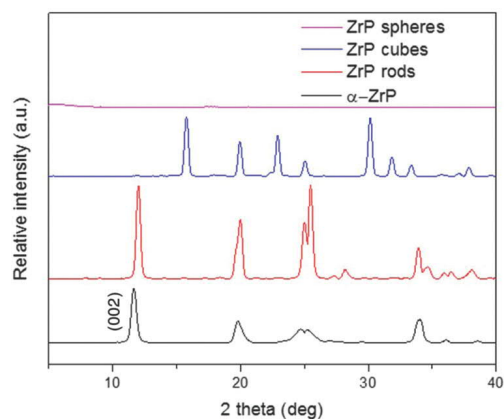


**Fig. 1** XRPD patterns of  $\alpha$ -ZrP, rod-like ZrP, cube-like ZrP ( $\tau'$ -ZrP), and spherical ZrP.

ture of  $\tau'$ -ZrP consist of the packing of these planes perpendicularly to each other. Our obtained XRPD pattern of  $\tau'$ -ZrP corresponds to the published XRPD pattern, with the presence of the characteristic  $17.9^\circ$  peak and the absence of the low intensity peaks at  $19.6^\circ$ ,  $30.6^\circ$ , and  $33.8^\circ$ . All other peaks are in accordance with the published XRPD pattern,<sup>24</sup> confirming the successful synthesis of the  $\tau'$ -ZrP phase. Fig. S1–S3† show the comparison of our experimental XRPD for the hexagonal, rod-like, and cube-like morphologies with their corresponding ICSD entries.

Fig. S4–S7† show the XRPD patterns of the ZrP samples with different morphologies (hexagonal platelets ( $\alpha$ -ZrP), rods, cubes ( $\tau'$ -ZrP), and spherical ZrP) after metal modification with Ni(II) and Co(II) cations. These patterns are identical to that of the ZrP samples before metal modification indicating that no significant changes in the structure of the support occurred; therefore, no intercalation of Ni(II) and Co(II) cations occurred during synthesis. In addition, no peaks corresponding to metal oxides are observed as the samples were not processed further, indicating either the small crystallite size of any produced metal oxide species or their amorphous nature.<sup>25</sup> To further characterize the different ZrP structures, we conducted IR spectroscopy measurements.

## FTIR

Fig. 2 shows the FTIR spectra of hexagonal shaped  $\alpha$ -ZrP, rod-like ZrP, cube-like ZrP, and spherical ZrP. The characteristic IR spectrum of  $\alpha$ -ZrP has four characteristic lattice water bands.<sup>42</sup> In our spectrum, these bands are observed at  $3594$ ,  $3508$ ,  $3143$  and  $1618\text{ cm}^{-1}$ . In addition, the symmetric and antisymmetric orthophosphate group vibrations in  $\alpha$ -ZrP are observed in the region of *ca.*  $1125$ – $929\text{ cm}^{-1}$ .<sup>42</sup> The FTIR spectrum of the rod-like ZrP is similar to that of  $\alpha$ -ZrP, but with a few notable changes. First, the four lattice water bands show a reduced relative intensity due to the higher temperature required for synthesis. In addition, two new bands are present at  $3212$  and  $1425\text{ cm}^{-1}$  which indicate the presence of  $\text{NH}_4^+$  ions.<sup>43,44</sup> The low intensity and broad band at  $3212\text{ cm}^{-1}$  can be attributed to the N–H asymmetric stretching and the one at  $1425\text{ cm}^{-1}$  to

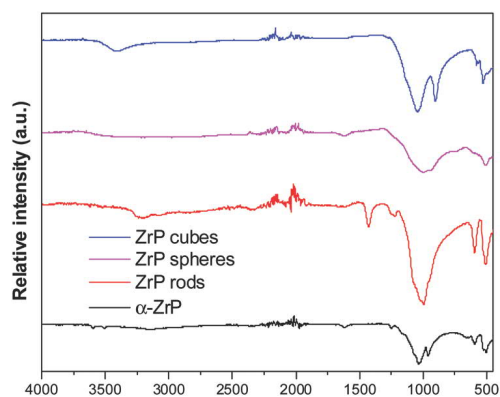


**Fig. 2** FTIR spectra of  $\alpha$ -ZrP, rod-like ZrP, spherical ZrP, and cube-like ZrP ( $\tau'$ -ZrP).

the H–N–H bending vibrational mode. This result suggests that even though  $\text{NH}_4^+$  did not intercalate into the ZrP layers (*vide supra*) there is a residual amount of  $\text{NH}_4^+$  remaining on the surface of the rods which stems from electrostatic interactions with the negatively charged surface. However, the presence of  $\text{NH}_4^+$  is minimal or in trace amounts as nitrogen is not detected in the EDS spectrum of the rod-like ZrP sample (Fig. S8†). The FTIR spectrum of the spherical ZrP only contains the orthophosphate group vibrations in the range of  $1166$ – $806\text{ cm}^{-1}$ . No water peaks are expected from this calcined sample. Finally, the spectrum of cube-like ZrP ( $\tau'$ -ZrP) shows the phosphate vibration modes in the range of  $1217$ – $856\text{ cm}^{-1}$  and a low intensity and broad band at  $3407\text{ cm}^{-1}$ . The latter may be attributed to O–H vibrational modes in the structure of  $\tau'$ -ZrP. The FTIR results show the expected peaks for the ZrP structures and showcase that no intercalation of nickel or cobalt cations occurred within the ZrP supports. To further characterize and assess the morphology of the as-prepared metal-modified structures, TEM/STEM was performed on pristine and metal-modified ZrP supports.

## TEM/STEM

Fig. 3 shows the TEM/STEM micrographs of  $\alpha$ -ZrP, rod-like ZrP, spherical ZrP, and cube-like ZrP ( $\tau'$ -ZrP). The  $\alpha$ -ZrP nanoparticles synthesized by the hydrothermal method show their characteristic hexagonal shape (Fig. 3a–c).<sup>20</sup> The micrographs of rod-like ZrP show that its particle length ranges from  $0.4$ – $0.8\text{ }\mu\text{m}$  with diameter of less than  $100\text{ nm}$  (Fig. 3d–f). However, as previously reported in the literature,<sup>23</sup> platelets are also observed in the micrographs. This result indicates that the synthesis method to produce rod-like ZrP results in ZrP. Particles with a mixture of morphologies. The ZrP spheres are large and uniform with diameters around  $1.5\text{ }\mu\text{m}$  (Fig. 3g–i). Nevertheless, larger spheres with diameters of  $2.0$ – $2.5\text{ }\mu\text{m}$  were also observed. The TEM/STEM micrographs for the cube-like ZrP show that the crystalline material size ranges from  $100$  to  $200\text{ nm}$  with their characteristic cube-like shape (Fig. 3j–l).<sup>24</sup> After modification with the metal cations, the morphology of the ZrP structures did not change (Fig. S9† shows the TEM/STEM micrographs for the cobalt-modified cube-like ZrP). The SEM images for the four morphologies are shown in Fig. S10† and their EDS spectra are shown in Fig. S11–S13.† The SEM micrographs show the expected morphologies while the EDS spectra show the expected elements on each sample. The presence of gold (Au) and carbon (C) in the EDS spectra is due to the Au coating used to increase sample conductivity and the carbon paper used to support the ZrP particles.

## ICP-MS

ICP-MS measurements (Table 1) were conducted to study the ion-exchange capacity (loading) of the Co and Ni modified ZrP supports. Since all supports were modified with an excess molar ratio of metal precursor ( $10 : 1\text{ M} : \text{ZrP}$ ), similar loadings were expected for all systems. Interestingly, ICP-MS studies show that each support differs in the maximum amount of

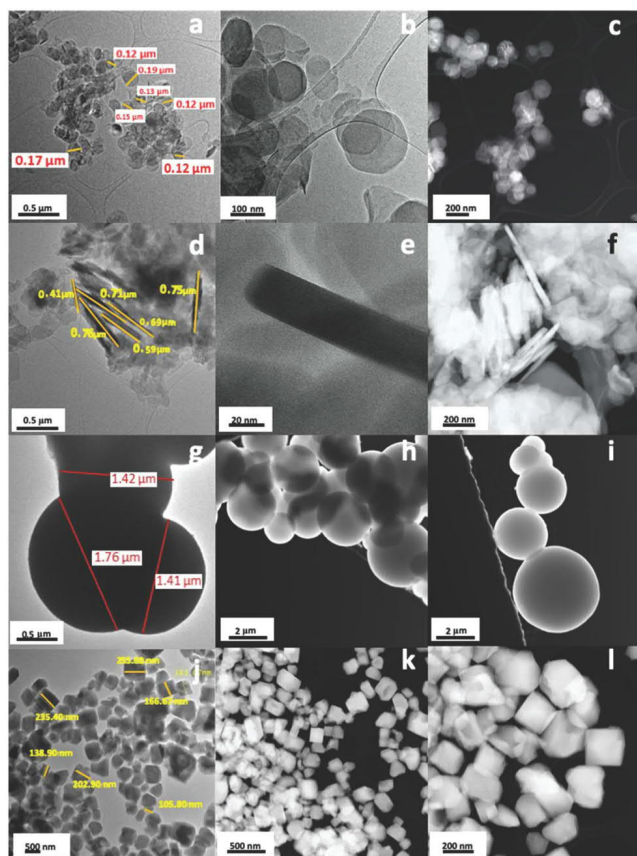


**Fig. 3** (a–c) TEM/STEM micrographs of  $\alpha$ -ZrP. Scale bars: 0.5  $\mu\text{m}$ , 100 nm, and 200 nm, respectively. (d–f) TEM/STEM micrographs of rod-like ZrP. Scale bars: 0.5  $\mu\text{m}$ , 20 nm, and 200 nm, respectively. (g–i) TEM/STEM micrographs of spherical ZrP. Scale bars: 0.5  $\mu\text{m}$ , 2  $\mu\text{m}$ , and 2  $\mu\text{m}$ , respectively. (j–l) TEM/STEM micrographs of cube-like ZrP. Scale bars: 200 nm, 500 nm, and 200 nm, respectively.

**Table 1** Selected electrochemical values and metal loading for the different metal-modified ZrP catalysts

Catalyst	Metal loading (%)	$\eta_3$ (V)	Tafel slope ( $\text{mV dec}^{-1}$ )	Mass activity @ $\eta = 500 \text{ mV}$ ( $\text{A g}^{-1}$ )
Co/ZrP $_{\alpha,\text{hexagonal}}$	1.86	0.451	79	6814
Co/ZrP $_{\text{rod}}$	1.79	0.451	79	5806
Co/ZrP $_{\text{cube}}$	0.75	0.496	82	4531
Co/ZrP $_{\text{sphere}}$	0.62	0.494	86	5478
Ni/ZrP $_{\alpha,\text{hexagonal}}$	1.25	0.592	132	684
Ni/ZrP $_{\text{rod}}$	0.91	0.600	127	552
Ni/ZrP $_{\text{cube}}$	0.45	0.640	134	1705
Ni/ZrP $_{\text{sphere}}$	0.42	0.460	67	11 745

metal species which can be ion-exchanged on the surface signifying that the number of possible Co or Ni active sites on each support varies from support to support and with the cation used during the ion-exchange process. Generally, cobalt cations exchange in a higher number when compared to nickel cations possibly due to the increased electronegativity of nickel in comparison to cobalt cations. Furthermore, both metal systems experience the same trend in maximum ion

exchange capacity for the various morphologies synthesized. The trends in maximum ion exchange capacity are  $\text{ZrP}_{\alpha,\text{hexagonal}} > \text{ZrP}_{\text{rods}} > \text{ZrP}_{\text{cubes}} > \text{ZrP}_{\text{spheres}}$ . A possible explanation for this phenomenon is the differences in particle size and crystallinity of the four ZrP structures. Previous work has found that particle size and crystallinity can affect the ion exchange behavior of zirconium phosphates.<sup>45</sup> However, the maximum ion exchange capacity trends achieved for the various ZrP structures are only for the specific synthesis conditions reported herein and factors, including, but not limited to, time, temperature, anion selection, particle size, crystallinity, solvent environment, and pH have been found to affect the ion-exchange capacity of zirconium phosphate systems.<sup>12,46,47</sup>

### Electrochemical measurements

All Ni(II) and Co(II)-modified ZrP catalysts were characterized for their OER electrochemical activity in an alkaline (0.1 M KOH) electrolyte. Linear sweep voltammetry was used to assess the OER activity. After metal modification, all ZrP support systems become electrochemically active for the OER (Fig. S14–S16<sup>†</sup>). Since no change in the XRPD patterns are observed after metal modification, the active species are deemed to be adsorbed at the surfaces and/or edges of the as-prepared structures, as previously observed.<sup>25</sup> Various reports have suggested that the primary figure of merit for OER is the overpotential at a current density of 10  $\text{mA cm}^{-2}$  on an electrode geometric area basis.<sup>40,48,49</sup> However, some of the catalysts in this study did not achieve this value at the potential range studied. Therefore, catalyst in this work are all compared at the overpotentials required to achieve a current density of 3  $\text{mA cm}^{-2}$  ( $\eta_3$ ).

Fig. 4a shows the linear sweep voltammograms of all Co/ZrP catalysts and the tabulated  $\eta_3$  values can be found in Table 1. The overpotential trends on an electrode geometric area basis for the different morphologies of the Co-modified catalysts are:  $\text{Co/ZrP}_{\alpha,\text{hexagonal}}$  (451 mV)  $\approx$   $\text{Co/ZrP}_{\text{rod}}$  (451 mV)  $<$   $\text{Co/ZrP}_{\text{sphere}}$  (494 mV)  $<$   $\text{Co/ZrP}_{\text{cube}}$  (496 mV).  $\text{Co/ZrP}_{\text{rod}}$  and  $\text{Co/ZrP}_{\alpha,\text{hexagonal}}$  have a similar metal content (Table 1); which partially explains their similar geometric activities. Fig. 4b shows the linear sweep voltammograms of all Ni/ZrP catalysts. For these Ni systems, the overpotential trends on a geometric basis for the various morphologies are  $\text{Ni/ZrP}_{\text{sphere}}$  (462 mV)  $<$   $\text{Ni/ZrP}_{\alpha,\text{hexagonal}}$  (592 mV)  $<$   $\text{Ni/ZrP}_{\text{rod}}$  (600 mV)  $<$   $\text{Ni/ZrP}_{\text{cube}}$  (640 mV). Our previous findings show that the difference in activity of two different metal-modified ZrP systems was due to a large difference in the metal content.<sup>26,50</sup> The higher geometric current density observed was attributed to the much higher metal content in metal-modified exfoliated ZrP catalysts compared to metal-modified  $\alpha$ -ZrP catalysts due to an increase in ion-exchange sites for exfoliated systems. For the Co/ZrP systems in this work, the geometric current density increases as the number of cobalt species increases. Conversely, as the number of nickel species increases, the geometric current density decreases; therefore, signifying that other factors are in play for the observed differences in the OER performance. To

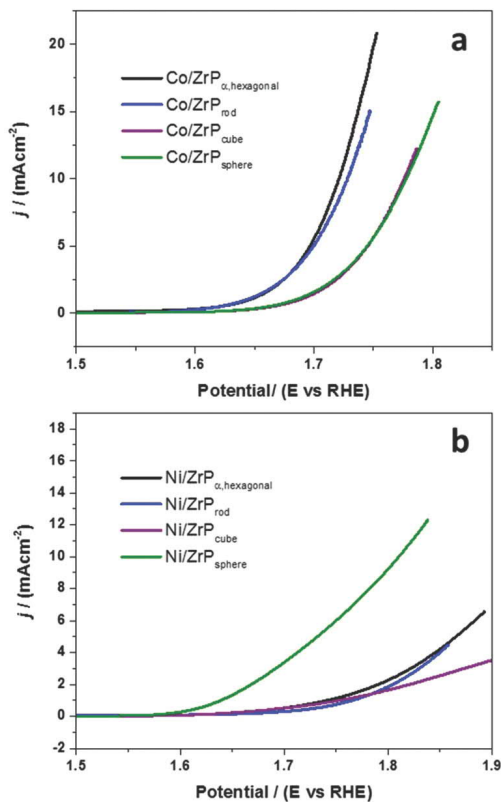


Fig. 4 Linear sweep voltammograms of (a) Co/ZrP catalysts and (b) Ni/ZrP catalysts.

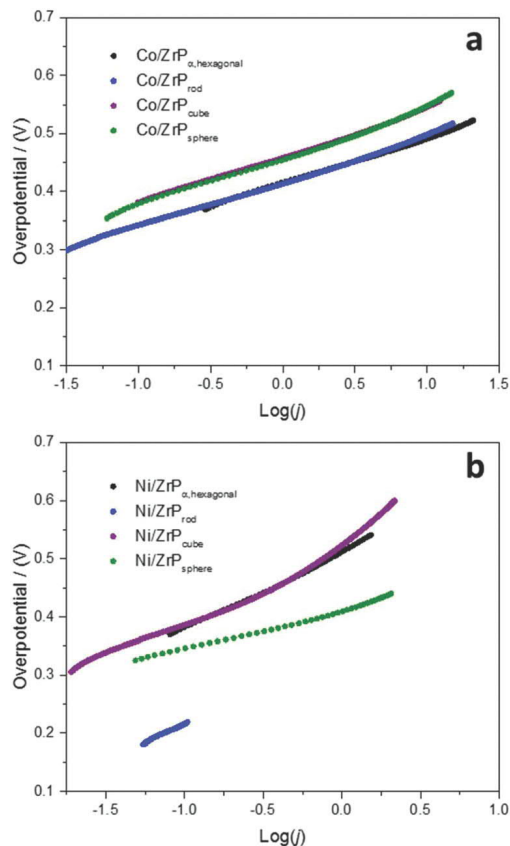


Fig. 5 Tafel plots of (a) Co/ZrP catalysts and (b) Ni/ZrP catalysts.

further investigate the activity of the Co/ZrP and Ni/ZrP catalysts, Tafel slopes were determined as an additional figure of merit for the comparison of the prepared catalysts.

Fig. 5a and b show the Tafel plots for all Co/ZrP and Ni/ZrP catalysts and the Tafel slope values can be found in Table 1. In general, the Tafel slopes of the Co/ZrP catalysts are similar ranging from 79–86  $\text{mV dec}^{-1}$ . For Ni/ZrP catalysts, the Tafel slopes are higher in comparison to Co/ZrP catalysts ranging from 127–134  $\text{mV dec}^{-1}$  with the exception of Ni/ZrP<sub>sphere</sub> with a Tafel slope of 67  $\text{mV dec}^{-1}$ . The differences in Tafel slopes may suggest differences in reaction mechanisms; however, further work would be necessary to ascertain mechanisms conclusively. In any event, trends in Tafel slopes and geometric area normalized activity alone are not sufficient to account for the intrinsic activity of electrocatalysts,<sup>51</sup> to this end we aimed to investigate mass-normalized catalytic activity.

To probe the intrinsic performance of these catalysts systems, the mass normalized activities for Co/ZrP and Ni/ZrP catalysts were determined from ICP-MS measurements and are shown in Fig. 6. Assuming all metal species are active for all Co/ZrP and Ni/ZrP structures, a mass activity comparison (evaluated at  $\eta = 500$  mV) in relation to geometric current activity trends is presented for the various ZrP structures and are tabulated in Table 1. For Co/ZrP structures, the trends in mass normalized currents are Co/ZrP<sub>α,hexagonal</sub> > Co/ZrP<sub>rod</sub> > Co/ZrP<sub>sphere</sub> > Co/ZrP<sub>cube</sub> and follow the same trends reported for geometric activity. For Ni/ZrP structures, the trends in mass normalized

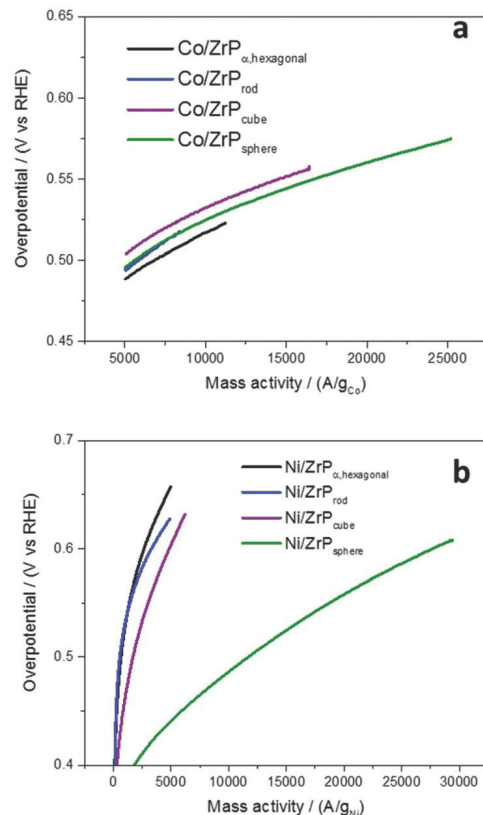


Fig. 6 Mass activity plots of (a) Co/ZrP catalysts and (b) Ni/ZrP catalysts.

currents, which are similar to geometric activity, are  $\text{Ni}/\text{ZrP}_{\text{sphere}} > \text{Ni}/\text{ZrP}_{\text{cube}} > \text{Ni}/\text{ZrP}_{\alpha,\text{hexagonal}} > \text{Ni}/\text{ZrP}_{\text{rod}}$  and, in comparison to  $\text{Co}/\text{ZrP}$  structures, the order in activity trends is reversed. A possible factor that could describe the reversal in activity trends between the two systems is conductivity. Previous work with cobalt and nickel species has shown that cobalt based systems have an effective conductivity 1–2 orders of magnitude higher at OER conditions over nickel based systems.<sup>52</sup> Furthermore, due to possible differences in conductivity, an analysis of physical characteristics such as the surface-area-to-volume ratio and the coverage of the metal species of the various metal-modified ZrP supports can assist in elucidating the reported activity trends.

First, cobalt-species on a geometric and mass basis appear to be more active on the structures made possible by  $\text{ZrP}_{\alpha,\text{hexagonal}}$  and  $\text{ZrP}_{\text{rods}}$ . One possible factor leading to this result is the improved surface-area-to-volume ratio (SA:V – see ESI† for calculation details) possible by the nanosized platelet morphology of  $\text{ZrP}_{\alpha,\text{hexagonal}}$  (SA:V = 0.07) and  $\text{ZrP}_{\text{rods}}$  (SA:V = 0.16) over  $\text{ZrP}_{\text{cubes}}$  (SA:V = 0.034) and  $\text{ZrP}_{\text{spheres}}$  (SA:V = 0.0039); therefore, cobalt-species obtain a high coverage on  $\alpha$ -ZrP and rod-like ZrP over the latter structures enabling improved electrocatalysis. Furthermore, four-point conductivity measurements (Fig. S14†) show that as the loading of cobalt species increases across the various structures, the conductivity of the composite materials is improved. These measurements suggest that the higher coverage of cobalt-species is not hindered by conductivity losses but improved instead; thus, a possible factor for the improved mass activity of cobalt species at higher loadings. However, we note that four-point probe conductivity measurements do not probe the *in situ* conductivity during OER but instead assess the in-plane conductivity of the catalysts powders in a compressed state. Therefore, these measurements are to be observed as an assumed proxy for the real conductivity of the metal-modified ZrP structures during catalysis. A similar analysis is presented for the  $\text{Ni}/\text{ZrP}$  structures. Four-point probe conductivity measurements show (Fig. S17†) that as the loading of Ni increases across these various structures, the conductivity of the composite materials is impaired. At higher nickel loadings, the abundance of resistive nickel species increases and due to the higher SA:V of  $\text{ZrP}_{\alpha,\text{hexagonal}}$  and  $\text{ZrP}_{\text{rods}}$ , it is possible that the higher coverage of Ni species leads to inactive areas on the surface of the ZrP structures. This higher coverage of resistive species can perturb the transport of electrons for the composite systems during electrocatalysis. Conversely, the surface area of  $\text{ZrP}_{\text{spheres}}$  is 1–2 orders of magnitude higher due to the micron size dimensions of the spheres; thus, the coverage of resistive nickel species is low and issues with conductivity are possibly minimized. Due to these possible factors, the improved mass activity of  $\text{Ni}/\text{ZrP}_{\text{cube}}$  and  $\text{Ni}/\text{ZrP}_{\text{sphere}}$  by 1–2 orders of magnitude over higher loading  $\text{Ni}/\text{ZrP}$  structures is possible. For comparison, Table S1† shows the mass activities and Tafel slopes reported herein with some state-of-the-art OER catalysts. Generally, the mass activities of the OER catalysts reported herein are lower than those state-of-the-art cata-

lysts. However, our  $\text{Ni}/\text{ZrP}_{\text{sphere}}$  catalyst shows a mass activity similar to that of  $\text{IrO}_x$ , highlighting the importance of loading and coverage of metal in the ZrP support. In contrast, the state-of-the-art  $\text{NiFeOxHy}$  catalyst shows a mass activity more than double that of our  $\text{Ni}/\text{ZrP}_{\text{sphere}}$  catalyst. This comparison suggests that designing new ZrP catalysts that contain mixed metals might improve the activity of these ZrP systems.

We conducted XPS measurements on our samples with the goal of further characterizing the composite materials herein. For both metal systems across various morphologies, XPS spectra showed no appreciable differences suggesting no apparent electronic metal-support interactions. For example Fig. S18A† shows the XPS spectra of the Co-modified ZrP samples in the Co 2p region; similar low intensity peaks are observed across all morphologies at binding energies approximately equal to the ones in our previous metal-modified ZrP report representative of Co in a mixed  $\text{Co}^{2+}/\text{Co}^{3+}$  state.<sup>25</sup> Fig. S18B† shows the XPS spectra of the Ni-modified ZrP samples in the Ni 2p region. Here we observe no appreciable signals, which we attribute to the even lower loading as Ni cations exchange in lower numbers than Co cations.

The data and analysis presented in this work showcases that the optimal loading and coverage of nickel and cobalt species on the various ZrP supports is crucial for improved OER activities. More specifically, the performance in terms of geometric and mass activities is found to increase with loading for cobalt systems and decrease with increased loading for nickel systems. Although the effective conductivity during OER was not measured, four-point probe conductivity measurements are used as a proxy and show that cobalt systems become more conductive with increased loading and nickel systems become more resistive with increased loading. These results suggest that the number of active sites involved in catalysis is changing on the various ZrP supports; therefore, the assumption that all sites are active for mass activity trends lead to conservative estimates for the real intrinsic activity of these systems.

Further experiments such as scanning electrochemical microscopy to determine the number of active sites per unit area, electrochemical measurements of the various metal-modified ZrP structures at similar loadings, and *in-operando* experiments such as X-ray absorption spectroscopy (XAS) will assist in quantifying and characterizing the Co and Ni species that are active during catalysis on the various ZrP structures.

## Conclusions

Our results elucidate the possible nature of the geometric and mass normalized activities of Co- and Ni-modified ZrP OER electrocatalysts in unique morphologies. We find that the loading and the coverage of cobalt and nickel species is important for optimal electrocatalysis. By modifying the morphology of the ZrP support, the maximum ion exchange capacities and coverage of nickel and cobalt cations is altered which directly influences the observed geometric and mass activity trends.

Thus, we can tune the OER activity by selection of the ZrP support and the metal used for its modification. Furthermore, a spherical ZrP morphology with low-loading nickel species showcases a mass activity that is 1–2 orders of magnitude higher over nickel species at higher loadings on hexagonal, rod, and cube-like ZrP structures. This work paves the way for future investigations for improving the activities of metal-modified ZrP by targeting improved conductivities of the as-synthesized composite materials. Follow up studies will be focused on improving OER activities by the co-ion exchange of multiple cations during the synthesis process to obtain bi-metallic ZrP systems.

## Conflicts of interest

There are no conflicts to declare.

## Acknowledgements

This work was supported by the National Science Foundation under the NSF-PREM Center for Interfacial Electrochemistry of Energy Materials (CIE2M) grant DMR-1827622, the NSF Center for Chemical Innovation in Solar Fuels CHE-1305124, and the Department of Energy SUNCAT Center for Interface Science and Catalysis DE-AC02-76SF00515. The single crystal X-ray diffractometer was acquired through the support of the NSF under the major instrumentation award CHE-1626103. M. V. R.-G. was supported by NSF-PREM CIE2 M, DMR-1827622. The authors would like to thank Eduardo Larios for the TEM/STEM micrographs, which were obtained at the Cornell Center for Materials Research (CCMR) facilities, NSF MRSEC grant No. DMR-1719875. Part of this work was performed at the Molecular Sciences Research Center of the University of Puerto Rico. The authors would also like to acknowledge the Materials Characterization Center of the University of Puerto Rico for the SEM micrographs and EDS spectra.

## Notes and references

- 1 A. Clearfield and J. A. Stynes, *J. Inorg. Nucl. Chem.*, 1964, **26**, 117–129, DOI: 10.1016/0022-1902(64)80238-4.
- 2 J. M. Troup and A. Clearfield, *Inorg. Chem.*, 1977, **16**, 3311–3314, DOI: 10.1021/ic50178a065.
- 3 G. Alberti, M. Casciola, U. Costantino and R. Vivani, *Adv. Mater.*, 1996, **8**, 291–303, DOI: 10.1002/adma.19960080405.
- 4 M. B. Santiago, C. Declet-Flores, A. Díaz, M. M. Vélez, M. Z. Bosques, Y. Sanakis and J. L. Colón, *Langmuir*, 2007, **23**, 7810–7817, DOI: 10.1021/la7005309.
- 5 M. B. Santiago, M. M. Vélez, S. Borrero, A. Díaz, C. A. Casillas, C. Hofmann, A. R. Guadalupe and J. L. Colón, *Electroanalysis*, 2006, **18**, 559–572, DOI: 10.1002/elan.200503432.
- 6 M. B. Santiago, G. A. Daniel, A. David, B. Casañas, G. Hernández, A. R. Guadalupe and J. L. Colón, *Electroanalysis*, 2010, **22**, 1097–1105, DOI: 10.1002/elan.200900329.
- 7 E. J. Rivera, C. Barbosa, R. Torres, L. Grove, S. Taylor, W. B. Connick, A. Clearfield and J. L. Colón, *J. Mater. Chem.*, 2011, **21**, 15899–15902, DOI: 10.1039/C1JM12053K.
- 8 E. J. Rivera, C. Figueroa, J. L. Colón, L. Grove and W. B. Connick, *Inorg. Chem.*, 2007, **46**, 8569–8576, DOI: 10.1021/ic7006183.
- 9 E. J. Rivera, C. Barbosa, R. Torres, H. Rivera, E. R. Fachini, T. W. Green, W. B. Connick and J. L. Colón, *Inorg. Chem.*, 2012, **51**, 2777–2784, DOI: 10.1021/ic201423q.
- 10 B. Casañas-Montes, A. Díaz, C. Barbosa, C. Ramos, C. Collazo, E. Meléndez, C. Queffelec, F. Fayon, A. Clearfield, B. Bujoli and J. L. Colón, *J. Organomet. Chem.*, 2015, **791**, 34–40, DOI: 10.1016/j.jorganchem.2015.05.031.
- 11 J. González-Villegas, Y. Kan, V. I. Bakhmutov, A. García-Vargas, M. Martínez, A. Clearfield and J. L. Colón, *Inorg. Chim. Acta*, 2017, **468**, 270–279, DOI: 10.1016/j.ica.2017.05.057.
- 12 A. Díaz, A. David, R. Pérez, M. L. González, A. Báez, S. E. Wark, P. Zhang, A. Clearfield and J. L. Colón, *Biomacromolecules*, 2010, **11**, 2465–2470, DOI: 10.1021/bm100659p.
- 13 A. Díaz, V. Saxena, J. González, A. David, B. Casañas, C. Carpenter, J. D. Batteas, J. L. Colón, A. Clearfield and M. D. Hussain, *Chem. Commun.*, 2012, **48**, 1754–1756, DOI: 10.1039/C2CC16218K.
- 14 A. Díaz, M. L. González, R. J. Pérez, A. David, A. Mukherjee, A. Báez, A. Clearfield and J. L. Colón, *Nanoscale*, 2013, **5**, 11456–11463, DOI: 10.1039/c3nr02206d.
- 15 Y. Zhou, R. Huang, F. Ding, A. D. Brittain, J. Liu, M. Zhang, M. Xiao, Y. Meng and L. Sun, *ACS Appl. Mater. Interfaces*, 2014, **6**, 7417–7425, DOI: 10.1021/am5008408.
- 16 M. Pica, *Catalysts*, 2017, **7**, 190, DOI: 10.3390/catal7060190.
- 17 A. Clearfield and D. S. Thakur, *Appl. Catal.*, 1986, **26**, 1–26, DOI: 10.1016/S0166-9834(00)82538-5.
- 18 H. Hu, J. C. Martin, M. Zhang, C. S. Southworth, M. Xiao, Y. Meng and L. Sun, *RSC Adv.*, 2012, **2**, 3810, DOI: 10.1039/c2ra00015f.
- 19 Y. Cheng and G. K. Chuah, *Chin. Chem. Lett.*, 2019, DOI: 10.1016/j.ccl.2019.04.063.
- 20 L. Sun, W. J. Boo, H.-J. Sue and A. Clearfield, *New J. Chem.*, 2007, **31**, 39–43, DOI: 10.1039/B604054C.
- 21 H. Xiao and S. Liu, *Mater. Des.*, 2018, **155**, 19–35, DOI: 10.1016/j.matdes.2018.05.041.
- 22 A. Tarafdar, A. B. Panda, N. C. Pradhan and P. Pramanik, *Microporous Mesoporous Mater.*, 2006, **95**, 360–365, DOI: 10.1016/j.micromeso.2006.05.008.
- 23 Y. Cheng, X. Wang, S. Jaenicke and G.-K. Chuah, *ChemSusChem*, 2017, **10**, 3235–3242, DOI: 10.1002/cssc.201700885.
- 24 M. Pica, R. Vivani, A. Donnadio, E. Troni, S. Fop and M. Casciola, *Inorg. Chem.*, 2015, **54**, 9146–9153, DOI: 10.1021/acs.inorgchem.5b01573.
- 25 J. Sanchez, M. V. Ramos-Garcés, I. Narkeviciute, J. L. Colón and T. F. Jaramillo, *Catalysts*, 2017, **7**, 132, DOI: 10.3390/catal7050132.

- 26 M. V. Ramos-Garcés, J. Sanchez, D. E. Del Toro-Pedrosa, I. B. Alvarez, Y. Wu, E. Valle, D. Villagrán, T. F. Jaramillo and J. L. Colón, *ACS Appl. Energy Mater.*, 2019, **2**, 3561–3567, DOI: 10.1021/acsaem.9b00299.
- 27 J. H. Montoya, L. C. Seitz, P. Chakthranont, A. Vojvodic, T. F. Jaramillo and J. K. Nørskov, *Nat. Mater.*, 2017, **16**, 70–81, DOI: 10.1038/nmat4778.
- 28 Y. Jiao, Y. Zheng, M. Jaroniec and S. Z. Qiao, *Chem. Soc. Rev.*, 2015, **44**, 2060–2086, DOI: 10.1039/C4CS00470A.
- 29 Z. W. Seh, J. Kibsgaard, C. F. Dickens, I. Chorkendorff, J. K. Nørskov and T. F. Jaramillo, *Science*, 2017, **355**, eaad4998, DOI: 10.1126/science.aad4998.
- 30 J. Wu, Y. Liu, D. Geng, H. Liu and X. Meng, *Int. J. Energy Res.*, 2018, **42**, 853–862, DOI: 10.1002/er.3862.
- 31 S. Zhao, B. Rasimick, W. Mustain and H. Xu, *Appl. Catal., B*, 2017, **203**, 138–145, DOI: 10.1016/j.apcatb.2016.09.048.
- 32 Y. Ding, A. Klyushin, X. Huang, T. Jones, D. Teschner, F. Girgsdies, T. Rodenas, R. Schlögl and S. Heumann, *Angew. Chem., Int. Ed.*, 2018, **57**, 3514–3518, DOI: 10.1002/anie.201711688.
- 33 J. W. D. Ng, Y. Gorlin, D. Nordlund and T. F. Jaramillo, *J. Electrochem. Soc.*, 2014, **161**, D3105–D3112, DOI: 10.1149/2.014407jes.
- 34 I. Narkeviciute and T. F. Jaramillo, *J. Phys. Chem. C*, 2017, **121**, 27295–27302, DOI: 10.1021/acs.jpcc.7b08690.
- 35 T. R. Hellstern, A. C. Nielander, P. Chakthranont, L. A. King, J. J. Willis, S. Xu, C. MacIsaac, C. Hahn, S. F. Bent, F. B. Prinz and T. F. Jaramillo, *ACS Appl. Nano Mater.*, 2019, **2**, 6–11, DOI: 10.1021/acsanm.8b01966.
- 36 A. L. Strickler, M. Escudero-Escribano and T. F. Jaramillo, *Nano Lett.*, 2017, **17**, 6040–6046, DOI: 10.1021/acs.nanolett.7b02357.
- 37 X. Li, X. Hao, A. Abudula and G. Guan, *J. Mater. Chem. A*, 2016, **4**, 11973–12000, DOI: 10.1039/C6TA02334G.
- 38 J. Sanchez, T. R. Hellstern, L. A. King and T. F. Jaramillo, *Adv. Energy Mater.*, 2019, 1901824, DOI: 10.1002/aenm.201901824.
- 39 T. Kijima, *Bull. Chem. Soc. Jpn.*, 1982, **55**, 3031–3032, DOI: 10.1246/bcsj.55.3031.
- 40 C. C. L. McCrory, S. Jung, J. C. Peters and T. F. Jaramillo, *J. Am. Chem. Soc.*, 2013, **135**, 16977–16987, DOI: 10.1021/ja407115p.
- 41 M. Pica, A. Donnadio, R. D'Amato, D. Capitani, M. Taddei and M. Casciola, *Inorg. Chem.*, 2014, **53**, 2222–2229, DOI: 10.1021/ic402884g.
- 42 S. E. Horsley, D. V. Nowell and D. T. Stewart, *Spectrochim. Acta, Part A*, 1974, **30**, 535–541, DOI: 10.1016/0584-8539(74)80093-0.
- 43 A. Echavarría and S. L. Amaya, *Powder Diffr.*, 2018, **33**, 315–318, DOI: 10.1017/S0885715618000672.
- 44 X. Wu, Y. Tao, L. Dong and J. Hong, *J. Mater. Chem.*, 2004, **14**, 901–904, DOI: 10.1039/B314775D.
- 45 A. Clearfield, *Annu. Rev. Mater. Sci.*, 1984, **14**, 205–229, DOI: 10.1146/annurev.ms.14.080184.001225.
- 46 A. A. Martí and J. L. Colón, *Inorg. Chem.*, 2003, **42**, 2830–2832, DOI: 10.1021/ic025548g.
- 47 A. Contreras-Ramirez, S. Tao, G. S. Day, V. I. Bakmutov, S. J. L. Billinge and H.-C. Zhou, *Inorg. Chem.*, 2019, **58**, 14260–14274, DOI: 10.1021/acs.inorgchem.9b02442.
- 48 C. C. L. McCrory, S. Jung, I. M. Ferrer, S. M. Chatman, J. C. Peters and T. F. Jaramillo, *J. Am. Chem. Soc.*, 2015, **137**, 4347–4357, DOI: 10.1021/ja510442p.
- 49 S. Jung, C. C. L. McCrory, I. M. Ferrer, J. C. Peters and T. F. Jaramillo, *J. Mater. Chem. A*, 2016, **4**, 3068–3076, DOI: 10.1039/C5TA07586F.
- 50 M. V. Ramos-Garcés, J. Sanchez, I. B. Alvarez, Y. Wu, D. Villagrán, T. F. Jaramillo and J. L. Colón, in *Water Chemistry*, ed. M. Eyvaz, IntechOpen, London, 2019. DOI: 10.5772/intechopen.88116.
- 51 S. Anantharaj and S. Kundu, *ACS Energy Lett.*, 2019, **4**, 1260–1264, DOI: 10.1021/acscenergylett.9b00686.
- 52 M. S. Burke, S. Zou, L. J. Enman, J. E. Kellon, C. A. Gabor, E. Pledger and S. W. Boettcher, *J. Phys. Chem. Lett.*, 2015, **6**, 3737–3742, DOI: 10.1021/acs.jpcclett.5b01650.